

Evaluating single-point quantitative magnetization transfer in the cervical spinal cord: Application to multiple sclerosis



Alex K. Smith^{a,b,c}, Samantha By^{a,b}, Bailey D. Lyttle^b, Richard D. Dortch^{b,d}, Bailey A. Box^b, Lydia J. McKeithan^{a,b}, Saakshi Thukral^{b,e}, Francesca Bagnato^{b,f}, Siddharama Pawate^{b,e}, Seth A. Smith^{a,b,d,*}

^a Department of Biomedical Engineering, Vanderbilt University, Nashville, TN, USA

^b Vanderbilt University Institute of Imaging Sciences, Vanderbilt University, Nashville, TN, USA

^c Functional MRI of the Brain Centre, Nuffield Department of Clinical Neurosciences, University of Oxford, Oxford, UK

^d Department of Radiology and Radiological Sciences, Vanderbilt University, Nashville, TN, USA

^e Merrol Hyde Magnet School, Hendersonville, TN, USA

^f Department of Neurology, Vanderbilt University, Nashville, TN, USA

ARTICLE INFO

Keywords:

Multiple sclerosis

Spinal cord

Normal appearing white matter

qMT

MT

ABSTRACT

Spinal cord (SC) damage is linked to clinical deficits in patients with multiple sclerosis (MS), however, conventional MRI methods are not specific to the underlying macromolecular tissue changes that may precede overt lesion detection. Single-point quantitative magnetization transfer (qMT) is a method that can provide high-resolution indices sensitive to underlying macromolecular composition in a clinically feasible scan time by reducing the number of MT-weighted acquisitions and utilizing a two-pool model constrained by empirically determined constants. As the single-point qMT method relies on a priori constraints, it has not been employed extensively in patients, where these constraints may vary, and thus, the biases inherent in this model have not been evaluated in a patient cohort. We, therefore, addressed the potential biases in the single point qMT model by acquiring qMT measurements in the cervical SC in patient and control cohorts and evaluated the differences between the control and patient-derived qMT constraints (k_{mf} , T_2R_{1f} , and T_{2m}) for the single point model. We determined that the macromolecular to free pool size ratio (PSR) differences between the control and patient-derived constraints are not significant ($p > 0.149$ in all cases). Additionally, the derived PSR for each cohort was compared, and we reported that the white matter PSR in healthy volunteers is significantly different from lesions ($p < 0.005$) and normal appearing white matter ($p < 0.02$) in all cases. The single point qMT method is thus a valuable method to quantitatively estimate white matter pathology in MS in a clinically feasible scan time.

1. Introduction

In patients with multiple sclerosis (MS), spinal cord (SC) damage is often thought to be responsible for a majority of clinically noted deficits (Ikuta and Zimmerman, 1976; Kearney et al., 2015a). The SC is less than one-tenth the size of the brain; thus, even small lesions can affect significant portions of the SC and in some cases even a small lesion in a white matter (WM) column can impair all function derived from that column. Radiologically, several studies have shown that SC pathology may provide a more direct indicator of disease progression and clinical disability than the brain can provide alone (Miller, 1994; Patrucco et al., 2012).

Conventional T_1 and T_2 magnetic resonance imaging (MRI) methods are sensitive to inflammatory and water content change in SC MS

disease (Gass et al., 1998) but not specific (Bergers et al., 2002) to axonal damage or demyelination. As a result, T_1 -weighted (T_1 -w) and T_2 -w MRI contrasts remain poor indicators of the static, severity of the disease and/or disease progression. Alternatively, magnetization transfer (MT) imaging has been shown to be sensitive to changes in myelin content, even in areas free from macroscopic lesions (Koenig, 1991; Kucharczyk et al., 1994; Schmierer et al., 2007).

Free water protons observed with conventional MRI methods (T_1 -w and T_2 -w imaging) are in exchange with protons associated with semi-immobile macromolecules in tissue (Wolff and Balaban, 1989) and thus MT is the biophysical phenomenon whereby an off-resonance (with respect to water) saturation is transferred to the free water from the semi-solid-like protons through dipole-dipole or direct chemical exchange. The magnitude of the MT effect has traditionally been

* Corresponding author at: 1161 21st Avenue South, Nashville, TN, USA.

E-mail address: seth.smith@vanderbilt.edu (S.A. Smith).

<http://dx.doi.org/10.1016/j.nicl.2017.07.010>

Received 30 January 2017; Received in revised form 3 July 2017; Accepted 12 July 2017

Available online 14 July 2017

2213-1582/ © 2017 Published by Elsevier Inc. This is an open access article under the CC BY-NC-ND license (<http://creativecommons.org/licenses/by-nc-nd/4.0/>).

quantified by the magnetization transfer ratio (MTR) and has been used in several studies to show that MT is correlated with myelin content (Filippi and Rocca, 2007; Laue et al., 2007; Schmierer et al., 2007). However, the MTR is only semi-quantitative and is significantly dependent on the MR acquisition parameters, as well as B_1 and B_0 inhomogeneities (Berry et al., 1999) and other non-MT-specific NMR parameters (Henkelman et al., 1993; Stanisz et al., 2005).

Some of the limitations of the MTR have been rectified by modeling (often via a two-pool model) the MT signal (Sled and Pike, 2000, 2001) as a function of offset-frequency of saturation and quantitatively deriving indices such as the macromolecular to free pool size ratio (PSR) and is termed quantitative MT (qMT). qMT typically utilizes several images at multiple RF irradiation powers and/or offsets, from which a so-called MT Z-spectrum can be generated for each voxel (Hinton and Bryant, 1996). In general, the measured Z-spectrum and associated fit (e.g. with a two-pool model – free [f] and macromolecular [m]) generate several indices, including the PSR (Dortch et al., 2010; Gochberg et al., 1997), the MT exchange rate from the macromolecular to pool to the free pool (k_{mf}), and the transverse and longitudinal relaxation rates for each pool (Stanisz et al., 2005). There is increased interest in estimating the PSR and several studies (Odrobina et al., 2005; Ou et al., 2009b; Rausch et al., 2009; Samsonov et al., 2012; Schmierer et al., 2007; Underhill et al., 2011) have shown a strong correlation between the PSR and white matter myelin density. Indeed, several studies of MS have incorporated qMT in the brain of MS patients showing association between the PSR and MR measures of myelin (Davies et al., 2004; Levesque et al., 2010; Tozer et al., 2003).

In principle, however, qMT studies have been limited by long acquisition times due to the need to collect multiple MT-weighted images, the demand for high signal to noise ratio (SNR), and thus, are difficult to implement clinically. Recently, fast whole-brain mapping of the PSR using only a single MT-weighted image (and a reference image) (Yarnykh, 2012) was developed and our group subsequently applied this method in the SC (Smith et al., 2014) and the thigh (Li et al., 2015) in healthy volunteers. This fast qMT estimation procedure (single-point qMT) is accomplished by utilizing expected or measured constraints on the individual indices that comprise the two-pool model (e.g. the exchange rate, macromolecular T_2 , and the combined value T_2R_1 of the water pool – see Yarnykh, 2012 for a full derivation of this model), providing an opportunity to sample fewer points along the MT z-spectrum and utilize the scan time savings for improved resolution or more rapid acquisitions. However, to date, the single point qMT has only been applied in one patient study in the brain of MS patients (Yarnykh et al., 2015) utilizing constraints derived from healthy volunteers alone.

We seek to further this work by assessing whether a set of healthy-cohort-derived constraints placed on the two-pool qMT model sufficiently captures the variation within patients with multiple sclerosis as

assessed in the cervical spinal cord of patients with MS, or whether it is necessary to derive individual patient-centered constraints to accurately estimate the PSR and its sensitivity to MS pathology.

2. Materials and methods

2.1. Data acquisition

The local Institutional Review Board approved this study, and signed informed consent was obtained prior to examination. Data were obtained from two cohorts: 1) thirteen healthy volunteers (8 males, age range 24–33 years, mean \pm standard deviation [SD] age 25 ± 2.5 years) and 2) eight relapsing-remitting MS (RRMS) patients (4 males, age range 30–49 years, mean \pm SD age 40.5 ± 5.37 years, median EDSS score = 0, range 0–3.5) along with a primary progressive MS (PPMS) patient (male, 60 years old, EDSS score 5). Some healthy volunteers overlapped with an existing qMT study (Smith et al., 2014). Table 2 provides relevant clinical and demographic characteristics of the patients.

All MRI data were acquired on a 3.0 tesla Philips Achieva scanner (Philips Healthcare, Best, The Netherlands, software versions R3.2.2.0 and R5.1.7.1). A quadrature body coil was used for excitation, and a 16-channel neurovascular coil was used for signal reception. The field-of-view (FOV) was centered between the C3 and C4 vertebral bodies and spanned, at minimum, the C2 to C5 vertebral levels in all subjects. Second-order shimming was used to minimize image artifacts arising from susceptibility differences between bone and tissue.

The same MT protocol from Smith et al. (2014) was used here: two MT pulse sequences were performed: 1) a low spatial resolution acquisition ($1 \times 1 \text{ mm}^2$) at 8 offsets ($\Delta\omega$) and 2 powers (α_{RF}) with a “full-fit” analysis (Yarnykh, 2002; Yarnykh and Yuan, 2004) and 2) a high-resolution acquisition ($0.65 \times 0.65 \text{ mm}^2$) at 1 offset and power to be used with a “single-point” analysis (Yarnykh, 2012). For the full-fit qMT experiment, MT-weighted images were acquired using a 3D MT-prepared spoiled gradient echo sequence (Sled and Pike, 2001) with a GRE readout and SENSE acceleration factor = 2 over 12 slices. Other parameters were: FOV = $150 \times 150 \text{ mm}^2$, and 2 signal averages. MT weighting was achieved using a 20-ms, single-lobed sinc pulse with Gaussian apodization (Smith et al., 2014). High-resolution, single-point MT-data were acquired using the same parameters, except a nominal in-plane resolution of $0.65 \times 0.65 \text{ mm}^2$ was applied with six signal averages. To correct for B_1 and B_0 inhomogeneities across the spinal cord, B_1 and B_0 maps were acquired using fast 3D techniques; T_1 mapping was performed using a multiple flip angle (MFA) acquisition. A high-resolution multi-echo gradient echo (mFFE) scan was also performed and all echoes were averaged to generate a high grey/white matter contrast target image for registration (Held et al., 2003). A detailed list of the sequence parameters is included in Table 1.

Table 1

Scan parameters and MT prepulse parameters for the high-resolution anatomical (mFFE), low- and high-resolution MT, B_1 , B_0 , and T_1 scans.

Scan	Resolution (mm^3)	Scan parameters	MT prepulse parameters		Scan time (m:ss)
			$\Delta\omega$ (kHz)	Powers	
mFFE	$0.65 \times 0.65 \times 5$	TR/TE ₁ /ΔTE/α: 700/7.2/8.8 ms/28°	–	–	5:30
Low-Res MT	$1 \times 1 \times 5$	TR/TE/α: 50/2.3 ms/6°	1, 1.5, 2, 2.5, 8, 16, 32, 100	360°, 820°	12:15
High-Res MT	$0.65 \times 0.65 \times 5$	TR/TE/α: 50/2.3 ms/6°	2.5, 100	820°	7:00
B ₁	$2 \times 2 \times 5$	TR ₁ /TR ₂ /TE/α: 30/130/2.8 ms/60°	–	–	1:12
B ₀	$2 \times 2 \times 5$	TR/TE ₁ /TE ₂ /α: 50/4.6/6.9 ms/60°	–	–	0:45
T ₁	$1.5 \times 1.5 \times 5$	TR/TE: 20/4.6 ms α: 5, 15, 20, 25, 30°	–	–	1:30
Total time:					28:12

Table 2

Relevant clinical and demographic characteristics for the nine patients with MS enrolled in this study. The vast majority of the patients had virtually no disability or minimal impairment, yet, 8/9 patients presented with at least 1 spinal cord lesion spanning the volume of interest of our study. The mean lesion volume over all patients with at least one lesion was found to be $152.38 \pm 81.16 \text{ mm}^3$.

Patient	Age	Sex	Years of MS	EDSS score	C-spine lesion locations	Lesion volume (mm^3) ^a
1	41	Male	8	0	C2–C4	210.46
2	44	Female	3	0	C4–C5	139.83
3	38	Female	11	0	C4	7.21
4	41	Female	4	3.5	C2–C4	219.11
5	40	Male	6	0	C2–C4	238.33
6	41	Female	15	1.0	N/A	0
7	49	Male	12	0	C3–C5	89.37
8	30	Male	7	0	C3–C5	104.27
9	60	Male	10	5.0	C2–C5	210.46

^a Measured using the ROIs drawn in the high resolution anatomical images.

Table 3

Median estimated parameter values for the k_{mf} , $T_{2f}R_{1f}$, and T_{2m} in the control and patient cohorts, and the p-value from the Kruskal-Wallis test comparing each parameter in each cohort over all slices.

	Control	Patient	p-Value
$k_{mf} (\text{s}^{-1})$	8.76	7.54	0.149
$T_{2f}R_{1f}$	0.0255	0.0279	0.355
$T_{2m} (\mu\text{s})$	10.51	10.26	0.576

2.2. Image processing

All data analyses were performed in MATLAB R2016a (Mathworks, Natick, MA). Prior to data fitting, all images were cropped to an area immediately around the SC and co-registered to the mFFE volume using the FLIRT package from FSL v5.0.2.1 (FMRIB, Oxford, UK) (Jenkinson et al., 2002; Jenkinson and Smith, 2001). The co-registration was applied on a slice by slice basis, utilized 2D rigid body registration, and was limited to translation and rotation ($\pm 5^\circ$) in-plane only (i.e. translation in x and y, and rotation about the z-axis). Additionally, the registration used a normalized correlation search cost, and spline interpolation. Following co-registration, qMT parameter maps were generated for each volunteer and patient using the full-fit qMT model described in Yarnykh (2002) & Yarnykh and Yuan (2004). This model contains six independent parameters: R_{1m} , R_{1f} , T_{2m} , T_{2f} , PSR = M_{0m}/M_{0f} , and $k_{mf} = k_{fm}/\text{PSR}$ (subscripts “f” and “m” represent “free water” and “macromolecular” pools, respectively). The $R_{1\text{obs}}$ ($1/T_{1\text{obs}}$) maps were independently reconstructed by fitting the MFA data to the SPGR signal equation in the steady-state (Fram et al., 1987); these maps were used during MT parameter estimation (below) to estimate the parameter R_{1f} (Yarnykh, 2002; Yarnykh and Yuan, 2004). Henkelman et al. (1993) & Morrison and Henkelman (1995) showed that the signal dependence on R_{1m} is weak; therefore, R_{1m} was set equal to the R_{1f} (Yarnykh, 2012). The remaining parameters were estimated for each voxel by fitting the full-fit qMT data to the above-described, two-pool MT model (Yarnykh, 2002; Yarnykh and Yuan, 2004). For all fitting, the nominal offset frequency and RF amplitudes were corrected in each

voxel using B_0 and B_1 maps, respectively.

It has been shown that k_{mf} , T_{2m} , and the product $T_{2f}R_{1f}$ can all be fixed during the fitting process because they all exhibit relatively constant values across tissues (Smith et al., 2014; Yarnykh, 2012). This results in a model with one free parameter, PSR, which can be estimated from qMT data at a single offset/power (plus a reference scan). To estimate reasonable fixed parameters values for the single-point qMT analysis, histograms of k_{mf} , T_{2m} , and $T_{2f}R_{1f}$ were created (see Section 2.3 below), and the median value of each parameter was chosen to enter into the single-point qMT analysis; the high-resolution MT-weighted images were then analyzed to estimate high-resolution PSR maps.

2.3. Single point constraints: controls vs patients

To determine whether the healthy control-derived (CD) constraints (assumptions) were similar to those from the MS patient-derived (PD) constraints, mean parameter values for $T_{2f}R_{1f}$, k_{mf} , and T_{2m} were calculated over each slice for each subject, and Kruskal-Wallis (nonparametric ANOVA) test was performed to evaluate if differences exist between cohorts for all estimated parameters. Next, to estimate reasonable fixed parameter values to enter the single-point qMT analysis, histograms of $T_{2f}R_{1f}$, k_{mf} , and T_{2m} that were derived from the full-fit analysis were created over the SC for all slices and for each cohort of subjects. The skewness of each histogram was also calculated, where a positive skewness indicates right-skewed data, while a negative skewness indicates left-skewed data. Lastly, the median value of each parameter from $T_{2f}R_{1f}$, k_{mf} , and T_{2m} in each cohort was determined. The calculated constraints (assumptions) from the control cohort were applied to the high-resolution control qMT data to derive the PSR maps. The calculated constraints from both cohorts (CD and PD) were used to estimate two sets of high-resolution PSR maps for the patient cohort.

2.4. Tissue segmentation

WM and grey matter (GM) tissues in the control cohort were segmented from the mFFE images using the multi-atlas segmentation tool (Asman and Landman, 2013) previously developed for mFFE acquisitions. Each GM/WM regions of interest (ROI) was eroded using the *imerode* tool (using a disk *strel* object with a radius of 1) from MATLAB to avoid partial volume effects and the mean PSR values from the single-point data were calculated voxel-by-voxel for each volunteer. An example segmentation is shown in Fig. 1a.

Since the multi-atlas procedure does not account for lesions, WM lesion (WM-L), normal appearing white matter (NAWM), and normal appearing grey matter (NAGM) ROIs in the patient cohort were drawn manually by two independent raters on the high-resolution mFFE image (shown in Fig. 1b and c). ROIs were placed manually using MIPAV (NIH, Bethesda, MD) for each slice of each subject. The ROIs were then eroded as for the healthy control multi-atlas method to ensure only the NAWM, NAGM, and WM-Ls were identified with minimal confounding effects from partial volume effects. The mean single-point PSR was calculated for each subject and tissue type (NAWM, NAGM, WM-L).

Table 4

Mean PSR values for white matter (WM), grey matter (GM) and WM lesion (WM-Ls) data.

			WM	GM	WM-Ls
Control PSR			0.19 ± 0.02	0.16 ± 0.02	N/A
Patient PSR	Control constraints	Rater 1	0.15 ± 0.02	0.13 ± 0.02	0.12 ± 0.03
		Rater 2	0.15 ± 0.03	0.13 ± 0.02	0.12 ± 0.03
	Patient constraints	Rater 1	0.15 ± 0.02	0.14 ± 0.02	0.12 ± 0.03
		Rater 2	0.16 ± 0.03	0.15 ± 0.03	0.13 ± 0.04

Table 5

Statistical comparisons (represented by p-values) between the healthy white matter (WM), and patient normal appearing white matter (NAWM) and WM lesions (WM-Ls) using the Wilcoxon rank-sum test for a single rater. Comparisons in the patient data are given for the PSR estimated from both the CD data and the PD data. Bolded values are considered significant results.

				CD PSR		PD PSR	
				NAWM	WM-Ls	NAWM	WM-Ls
	Healthy WM	1	Healthy GM				
CD PSR	Healthy WM		< 0.001	< 0.001	< 0.001	0.011	0.003
	NAWM			1	0.015	0.190	0.036
PD PSR	WM-Ls				1	0.011	0.328
	NAWM					1	0.015
	WM-Ls						1

2.5. Statistical analysis of patient and control single point PSR

Statistical comparisons were performed on the mean PSR values between i) raters for the patient cohort using the PSR estimated from the patient-derived constraints, ii) each tissue type in the patient cohort (NAWM, NAGM, and WM-Ls) using both sets of derived constraints (CD and PD), and iii) the healthy control cohort (WM and GM) and the patient cohort for each tissue type and set of constraints. A significance threshold of $p < 0.05$ was chosen for all statistical comparisons. The Wilcoxon rank-sum test was used for comparisons ii) and iii), while the Bland-Altman analysis (Bland and Altman, 1986), consisting of the normalized Bland-Altman difference (D_{BA}), 95% confidence interval for the difference, and the limits of agreement ($1.96 \times SD$ of the difference across scans), was used for the inter-rater comparisons in i).

3. Results

3.1. Comparison of control and patient single point constraints

The histograms derived from the low-resolution, full fit qMT analysis for k_{mf} , $T_{2f}R_{1f}$, and T_{2m} over the whole cervical cord are shown in Fig. 2 for both the control and patient groups. None of the parameter estimates were found to be significantly different between controls and patients (p-values: $k_{mf} = 0.149$, $T_{2f}R_{1f} = 0.355$, $T_{2m} = 0.576$). All histograms are single-peaked and show similar skewness between cohorts – the k_{mf} (skewness: CD – 2.11, PD – 2.04) and $T_{2f}R_{1f}$ (skewness: CD – 2.40, PD – 2.19) are skewed to the left with long tails at high values, while the T_{2m} presents little to no skew (skewness: CD – 0.65, PD – 0.50). The median values for the control and patient cohorts are: $[8.76, 7.54] s^{-1}$, $[0.0255, 0.0279]$, and $[10.66, 10.51] \mu s$ for the k_{mf} , $T_{2f}R_{1f}$, and T_{2m} , respectively, and are also shown in Table 3.

3.2. High-resolution single point data

Anatomical images, R_{1obs} maps, and PSR maps are displayed in Fig. 3 for a healthy control and a patient with MS, where the constraints

derived from the patient population were used to generate the PSR values. Note that the contrast in the PSR is such that WM areas have a higher PSR value (yellow-red) than GM (green), while the CSF exhibits little to no MT effect (dark blue). The average T_{1obs} values for the healthy GM and WM are $[GM: 1.37 \pm 0.08 s, WM: 1.28 \pm 0.08 s]$, while the average T_{1obs} values in the patient GM, NAWM, and lesions are: $[GM: 1.49 \pm 0.16 s, NAWM: 1.38 \pm 0.14 s, Lesions: 1.49 \pm 0.19 s]$. Several differences can be appreciated when the PSR in the healthy control and patient are compared. In areas associated with a lesion on the anatomical image, we see a decrease in the PSR of the patient (0.11 ± 0.03); this is reduced compared to the NAWM (0.14 ± 0.04), and the control WM (0.18 ± 0.03) PSR.

The Bland-Altman plots for the inter-rater comparison are displayed in Fig. 4. The 95% confidence intervals for all tissues overlap zero, indicating there are no significant differences between raters. Furthermore, the limits of agreement in the NAWM (Fig. 4a) and GM (Fig. 4b) are within $\pm 1.5\%$, which is within one standard deviation of the mean PSR over all patients (see Table 4). The lesions had the largest 95% confidence intervals and limits of agreement, indicating that the delineation of lesion boundaries produced the largest variation between raters. However, none of the tissue types were shown to be significantly different (p-values: NAWM – 0.480, GM – 0.07, WM-Ls – 0.337); therefore, all subsequent analyses use only the ROIs taken from rater 1.

Mean single-point PSR values for the healthy controls and MS patient groups are shown in Table 4. In all cases the healthy PSR (WM: 0.19 ± 0.02 , GM: 0.16 ± 0.02) was found to be higher than the patient PSR (CD – NAWM: 0.15 ± 0.02 , NAGM: 0.13 ± 0.02) for each respective tissue class. The lesion data displayed similar PSR values (CD WM-Ls: 0.13 ± 0.03) to the NAGM over all patients, and was in all cases lower than the PSR of the healthy WM and patient NAWM.

The statistical comparisons between the healthy and patient cohorts from the Wilcoxon rank-sum test are displayed in Table 5 for WM. The WM in the healthy controls was significantly different from both CD and PD PSR for all tissue types (p-values < 0.01 for WM-Ls, p-values < 0.05 for NAWM). Additionally, the NAWM was found to be significantly different from lesions ($p < 0.05$) in all cases. The CD

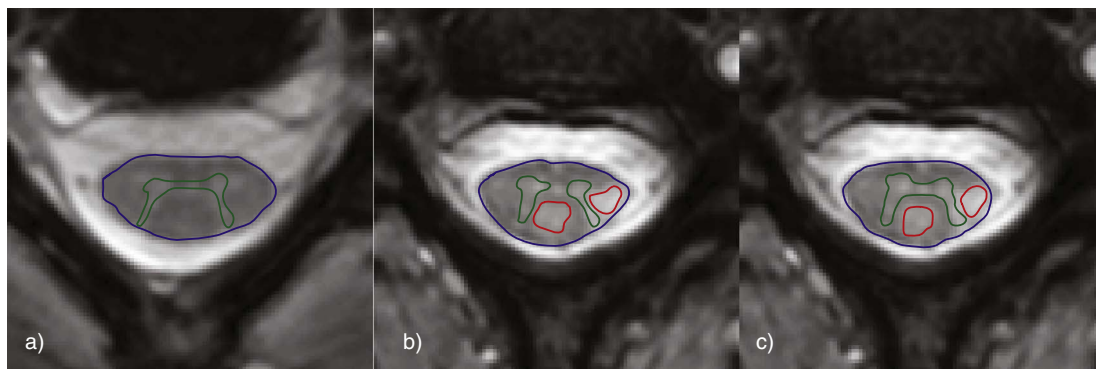


Fig. 1. High-resolution anatomical images in a healthy control (a.), and an MS patient for rater #1 (b.) and rater #2 (c.) with ROIs drawn for NAWM (blue), NAGM (green), and WM-Ls (red). (For interpretation of the references to color in this figure legend, the reader is referred to the web version of this article.)

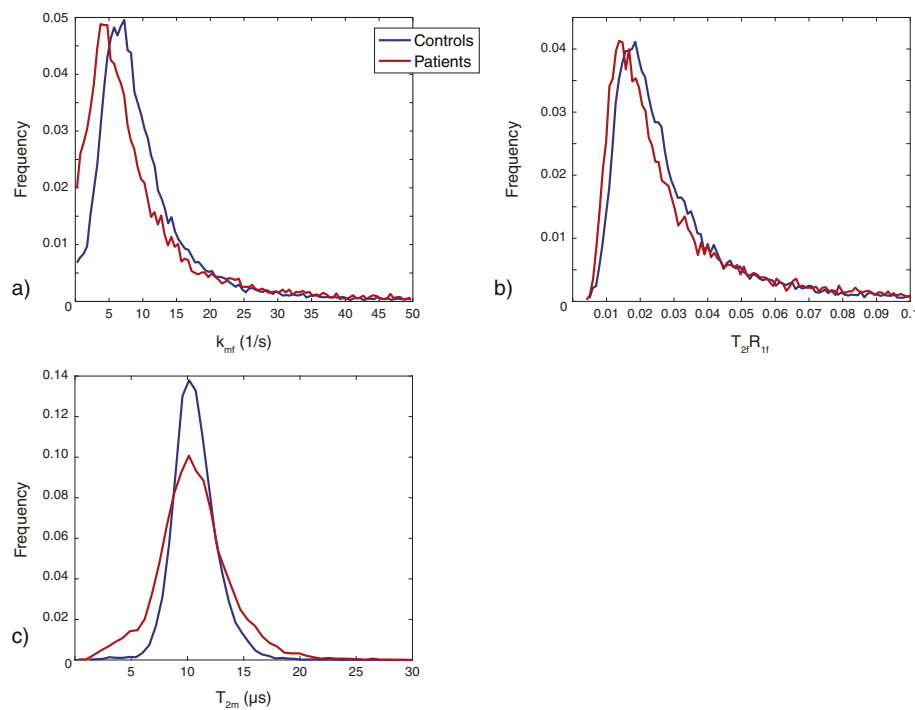


Fig. 2. Parameter histograms over the whole cervical SC for the healthy controls (blue) and patients (red) derived from (a.) the exchange rate, k_{mf} , (b.) the $T_{2f}R_{1f}$, and (c.) the T_{2m} . (For interpretation of the references to color in this figure legend, the reader is referred to the web version of this article.)

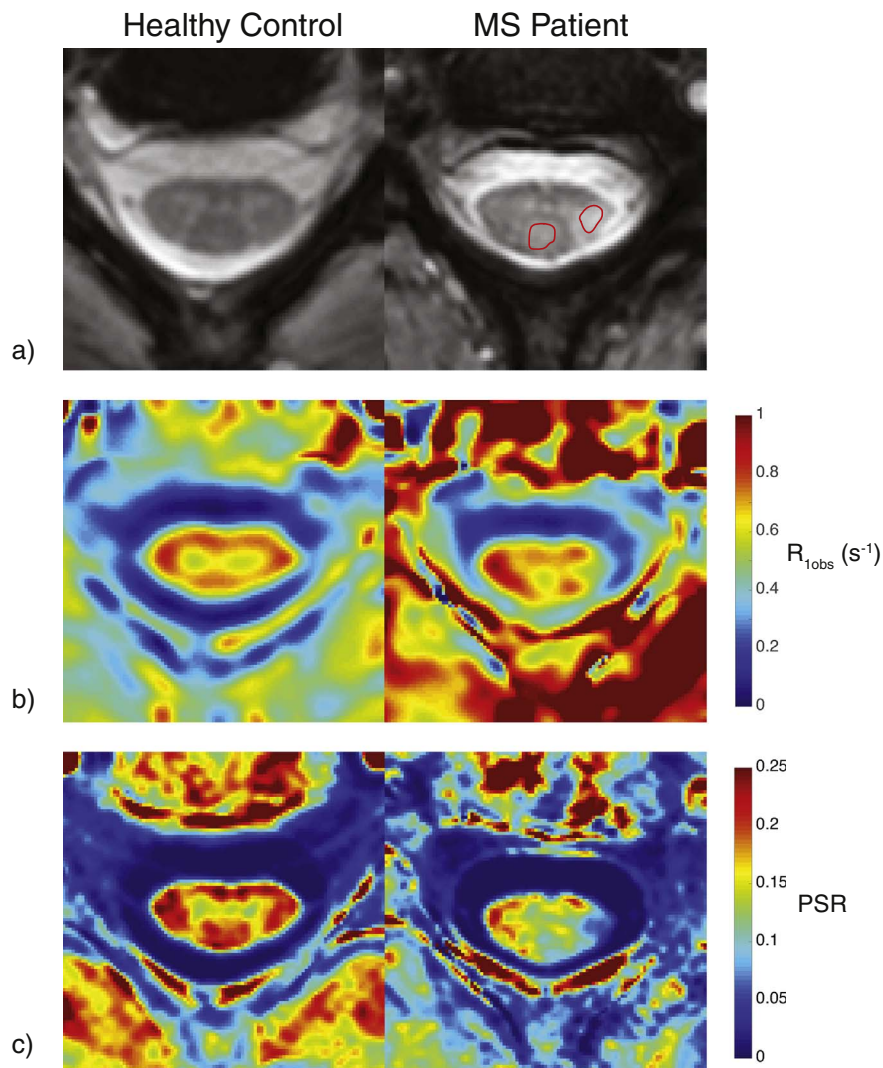


Fig. 3. Anatomical data (a.), R_{1obs} (b.), and PSR (c.) data for a typical healthy control and patient with MS (using the patient-derived parameters). Notice the decreased PSR over areas where a lesion is present, and in the areas surrounding these lesions (lesions outlined in red). (For interpretation of the references to color in this figure, the reader is referred to the web version of this article.)

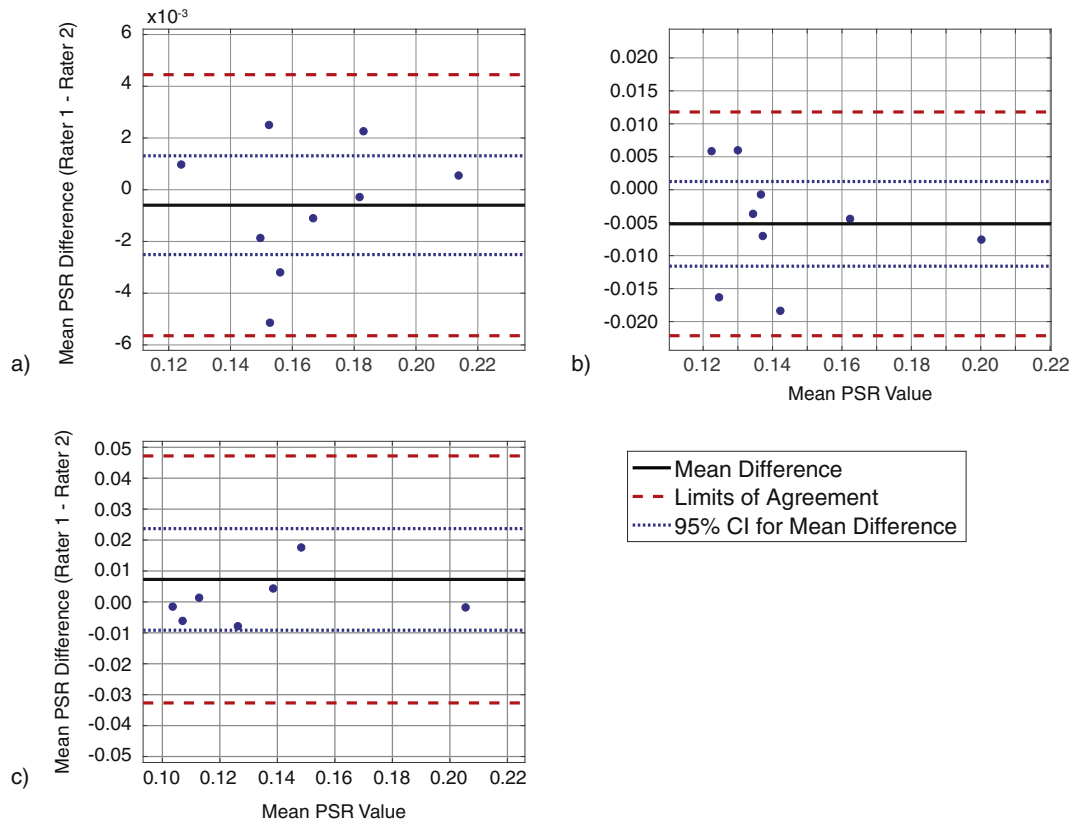


Fig. 4. Bland-Altman plots for the inter-rater reproducibility in the (a.) normal appearing white matter (NAWM), (b.) grey matter (GM), and (c.) WM lesion (WM-Ls) in the MS patients using the PSR calculated from the patient-derived constraints. The Bland-Altman differences and p-values for the NAWM, GM, and WM-Ls are [0.398, 0.480], [3.975, 0.07], and [5.51, 0.337], respectively.

NAGM PSR data was found to be significantly different from the healthy GM ($p = 0.008$), while the PD NAGM only approached a significant value. No significant differences were observed between the PD and CD PSR data in NAWM, NAGM, or WM-L ($p > 0.15$ in all cases). This demonstrates that the small differences seen in k_{mf} did not significantly affect the single point model when it was applied to a patient cohort.

4. Discussion

The goal of this study was to evaluate how assumed constraints derived from a full qMT analysis, and applied to a single-point qMT method, are different in pathology, such as in MS. We compared the calculated constraints for each population (healthy controls and patients with MS) and evaluated the PSR across patients (using both CD and PD assumptions) in the NAWM, NAGM, and WM-Ls, as well as between MS patients and healthy controls. We demonstrated that the error observed in the full fit analysis for MS patients does not significantly bias the PSR calculations derived from the single point methodology.

To the best of our knowledge, this is the first study to perform a full qMT analysis in the SC of patients with MS and evaluating the validity of the single-point assumptions. Therefore our results, although preliminary, show important and novel conclusions. The observed k_{mf} in patients was found to be 7.54 s^{-1} , which is lower than what has been observed in healthy controls ($k_{mf} = 8.76 \text{ s}^{-1}$). Additionally, the T_{1obs} was found to be higher in WM-Ls, compared to NAWM and healthy WM, which is expected, and incorporated into the two-pool qMT model. Therefore, our results suggest that the observed PSR changes are driven by macromolecular content rather than inflammation (Odrobina et al., 2005; Schmierer et al., 2007). Nevertheless, one shall keep in mind that these changes may also be due to increased water content present in advanced WM-Ls where a high degree of tissue loss is present relative to

other tissues, which would decrease both the PSR and k_{mf} , and increase the T_1 . Laule et al. (2016) recently demonstrated that the myelin water fraction (MWF) is significantly decreased in postmortem lesions relative to NAWM and patient GM, which may explain the observed changes in T_1 and exchange rate in patients with MS relative to healthy controls.

A potential source of bias in the above analysis is caused by using median, whole-cord values for the single point constraints (e.g. k_{mf} , $T_{2fR_{1f}}$, and T_{2m}), as the heterogeneity present in the NAWM, NAGM, and WM-Ls may be removed. Therefore, ROIs were also drawn in the low-resolution data for each tissue type (NAWM, NAGM, and WM-Ls), and the mean parameter values were found for each subject and tissue type. The Wilcoxon rank-sum test was performed between each patient tissue type and the mean whole-cord control data. No significant differences were found between the tissue-specific patient data and the control data ($p > 0.15$ in all cases). This is an important characterization, as it further indicates that the k_{mf} , $T_{2fR_{1f}}$, and T_{2m} are not sensitive to MS-induced changes, signifying that the PSR alone is an indicator of macromolecular changes in the CNS.

The high resolution PSR data in Table 5 and Fig. 3 demonstrated significant differences between healthy WM PSR and NAWM, NAGM, and WM-Ls PSR in patients. Furthermore, the changes due to exchange rate seen from the full fit data do not present a significant difference in PSR between the CD and PD patient data. This indicates that there may be pathological changes to the neurological tissues that cannot be visualized in the anatomical data. As MT has been shown to visualize the underlying macromolecular tissue dynamics within tissues (Odrobina et al., 2005; Ou et al., 2009a; Schmierer et al., 2007), these changes may reflect underlying neurological tissue changes that occur prior to more overt radiological symptoms seen in conventional imaging methodologies.

An important aspect of the PSR is its sensitivity to macromolecular-

induced changes in WM. Therefore, detecting WM changes along the spinal cord would provide substantial benefits to researchers and clinicians, as the PSR could then be used to track how lesions may be affecting NAWM caudal to the lesion site. To this end, we compared how the PSR changed along the spinal cord in the patient cohort. We used the Kruskal-Wallis test (nonparametric ANOVA) to determine if the variation along the spinal cord was greater than the variation between patients for both NAWM and NAGM. Although the NAGM did not show significant differences ($p = 0.26$), significant differences were observed for the NAWM ($p < 0.05$). In particular, near C2/C3, the NAWM PSR was approximately 0.161 ± 0.024 , while the NAWM PSR was approximately 0.127 ± 0.026 near C5/C6. We have demonstrated previously (Smith et al., 2014) that the PSR does not display regional variations in healthy volunteers. Therefore, the PSR may be detecting regional changes in the macromolecular content due to pathology. However, further research utilizing a larger patient population is needed in order to confirm this hypothesis.

GM demyelination has recently become a topic of interest when evaluating radiological and clinical deficits associated with MS. Gilmore et al. (2006) reported evidence of GM demyelination in post-mortem studies of patients with MS, and found a significantly greater proportion of demyelinated GM compared with WM. Kearney et al. (2015b, 2013) reported GM involvement in multiple studies; this suggests that GM may be significantly affected by MS in the SC. Here, we confirm these post mortem findings with our in vivo measurements. NAGM in patients had significantly different qMT-derived measures than that of healthy persons.

The patient group introduced in this work was on average 15 years older than the respective control group, which may have contributed to some of the differences between the WM and NAWM. Indeed, a study has shown age-related changes in the MTR (Ge et al., 2002), which may translate to the PSR. While this study demonstrated that there were no significant differences between the CD and PD single point qMT constraints, there may be changes in the PSR due to age, which may bias any conclusions that are drawn from the data. Therefore, future studies should seek to compare patient data to age-matched control data to ensure changes are due to pathology alone.

Although the patients in this study presented with multiple focal lesions, their clinical disability scores were fairly low. While the highest Expanded Disability Status Scale (EDSS) score in the patient cohort was 5, most of the patients had EDSS scores of 1 or 0, which biases correlations that could be performed. Addressing the impact of our qMT-derived measures on clinical disability was outside the scope of this work which was not powered towards that. Nevertheless, this is the next logical continuation of this study. Our group is already expanding the work to a larger cohort of MS patients with a more heterogeneous clinical expression of the disease to assess the clinical implications of our imaging findings.

5. Conclusions

This study demonstrated that a set of control-derived constraints can be used to accurately map PSR data in patients with MS. Our results also demonstrate that the PSR is an important tool to quantify MS, and may provide a more stable measure of the effects of demyelination and axonal damage than can be provided through conventional imaging alone. Developing clinically-oriented metrics to quantify tissue pathologies may offer additional insights into disease diagnosis and progression.

Acknowledgements

We would like to thank Ms. Kristen George-Durrett, Ms. Clair Jones, Ms. Leslie McIntosh, and Mr. Chris Thompson, who have provided invaluable assistance with scheduling, subject assistance, and data collection. We would also like to thank the healthy volunteers and patients

with MS for donating their time, which allowed us to perform this study. This work was supported by: NIH/NIBIB K01 EB009120, NIH/NIBIB K25 EB013659, NIH/NCI R25 CA136440, NIH/NIBIB R01 EY023240 01A1, NIH/NINDS R21 NS087465-01, and DOD W81XWH-13-0073. Portions of this study were also funded by the National Multiple Sclerosis Society (NMSS RG-1501-02840).

References

- Asman, A.J., Landman, B.A., 2013. Non-local statistical label fusion for multi-atlas segmentation. *Med. Image Anal.* 17, 194–208.
- Bergers, E., Bot, J.C., De Groot, C.J., Polman, C.H., Lycklama A Nijeholt, G.J., Castelijns, J.A., van der Valk, P., Barkhof, F., 2002. Axonal damage in the spinal cord of MS patients occurs largely independent of T2 MRI lesions. *Neurology* 59, 1766–1771.
- Berry, I., Barker, G.J., Barkhof, F., Campi, A., Dousset, V., Franconi, J.M., Gass, A., Schreiber, W., Miller, D.H., Tofts, P.S., 1999. A multicenter measurement of magnetization transfer ratio in normal white matter. *J. Magn. Reson. Imaging* 9, 441–446.
- Bland, J.M., Altman, D.G., 1986. Statistical methods for assessing agreement between two methods of clinical measurement. *Lancet* 1, 307–310.
- Davies, G.R., Tozer, D.J., Cercignani, M., Ramani, A., Dalton, C.M., Thompson, A.J., Barker, G.J., Tofts, P.S., Miller, D.H., 2004. Estimation of the macromolecular proton fraction and bound pool T2 in multiple sclerosis. *Mult. Scler.* 10, 607–613.
- Dortch, R.D., Welch, E.B., Gore, J.C., Smith, S.A., 2010. Quantitative Magnetization Transfer Imaging of Human Cervical Spinal Cord at 3T. ISMRM Annual Meeting (Hawaii).
- Filippi, M., Rocca, M.A., 2007. Magnetization transfer magnetic resonance imaging of the brain, spinal cord, and optic nerve. *Neurotherapeutics* 4, 401–413.
- Fram, E.K., Herfkens, R.J., Johnson, G.A., Glover, G.H., Karis, J.P., Shimakawa, A., Perkins, T.G., Pelc, N.J., 1987. Rapid calculation of T1 using variable flip angle gradient refocused imaging. *Magn. Reson. Imaging* 5, 201–208.
- Gass, A., Filippi, M., Rodegher, M., Schwartz, A., Comi, G., Hennerici, M., 1998. Characteristics of chronic MS lesions in the cerebrum, brainstem, spinal cord, and optic nerve on T1-weighted MRI. *Neurology* 50, 548–550.
- Ge, Y., Grossman, R.I., Babb, J.S., Rabin, M.L., Mannon, L.J., Kolson, D.L., 2002. Age-related total gray matter and white matter changes in normal adult brain. Part II: quantitative magnetization transfer ratio histogram analysis. *AJNR Am. J. Neuroradiol.* 23, 1334–1341.
- Gilmore, C.P., Bo, L., Owens, T., Lowe, J., Esiri, M.M., Evangelou, N., 2006. Spinal cord gray matter demyelination in multiple sclerosis—a novel pattern of residual plaque morphology. *Brain Pathol.* 16, 202–208.
- Gochberg, D.F., Kennan, R.P., Gore, J.C., 1997. Quantitative studies of magnetization transfer by selective excitation and T1 recovery. *Magn. Reson. Med.* 38, 224–231.
- Held, P., Dorenbeck, U., Seitz, J., Frund, R., Albrich, H., 2003. MRI of the abnormal cervical spinal cord using 2D spoiled gradient echo multiecho sequence (MEDIC) with magnetization transfer saturation pulse. A T2* weighted feasibility study. *J. Neuroradiol.* 30, 83–90.
- Henkelman, R.M., Huang, X., Xiang, Q.S., Stanisz, G.J., Swanson, S.D., Bronskill, M.J., 1993. Quantitative interpretation of magnetization transfer. *Magn. Reson. Med.* 29, 759–766.
- Hinton, D.P., Bryant, R.G., 1996. 1H magnetic cross-relaxation between multiple solvent components and rotationally immobilized protein. *Magn. Reson. Med.* 35, 497–505.
- Ikuta, F., Zimmerman, H.M., 1976. Distribution of plaques in seventy autopsy cases of multiple sclerosis in the United States. *Neurology* 26, 26–28.
- Jenkinson, M., Smith, S., 2001. A global optimisation method for robust affine registration of brain images. *Med. Image Anal.* 5, 143–156.
- Jenkinson, M., Bannister, P., Brady, M., Smith, S., 2002. Improved optimization for the robust and accurate linear registration and motion correction of brain images. *NeuroImage* 17, 825–841.
- Kearney, H., Miszkil, K.A., Yiannakas, M.C., Ciccarelli, O., Miller, D.H., 2013. A pilot MRI study of white and grey matter involvement by multiple sclerosis spinal cord lesions. *Mult. Scler. Relat. Disord.* 2, 6.
- Kearney, H., Miller, D.H., Ciccarelli, O., 2015a. Spinal cord MRI in multiple sclerosis—diagnostic, prognostic and clinical value. *Nat. Rev. Neurol.* 11, 327–338.
- Kearney, H., Miszkil, K.A., Yiannakas, M.C., Altmann, D.R., Ciccarelli, O., Miller, D.H., 2015b. Grey matter involvement by focal cervical spinal cord lesions is associated with progressive multiple sclerosis. *Mult. Scler.*
- Koenig, S.H., 1991. Cholesterol of myelin is the determinant of gray-white contrast in MRI of brain. *Magn. Reson. Med.* 20, 285–291.
- Kucharczyk, W., Macdonald, P.M., Stanisz, G.J., Henkelman, R.M., 1994. Relaxivity and magnetization transfer of white matter lipids at MR imaging: importance of cerebrospinal fluid and pH. *Radiology* 192, 521–529.
- Laule, C., Vavasour, I.M., Kolind, S.H., Li, D.K., Traboulsee, T.L., Moore, G.R., MacKay, A.L., 2007. Magnetic resonance imaging of myelin. *Neurotherapeutics* 4, 460–484.
- Laule, C., Yung, A., Pavolva, V., Bohnet, B., Kozłowski, P., Hashimoto, S.A., Yip, S., Li, D.K., Moore, G.W., 2016. High-resolution myelin water imaging in post-mortem multiple sclerosis spinal cord: a case report. *Mult. Scler.*
- Levesque, I.R., Giacomini, P.S., Narayanan, S., Ribeiro, L.T., Sled, J.G., Arnold, D.L., Pike, G.B., 2010. Quantitative magnetization transfer and myelin water imaging of the evolution of acute multiple sclerosis lesions. *Magn. Reson. Med.* 63, 633–640.
- Li, K., Dortch, R.D., Kroop, S.F., Huston, J.W., Gochberg, D.F., Park, J.H., Damon, B.M., 2015. A rapid approach for quantitative magnetization transfer imaging in thigh muscles using the pulsed saturation method. *Magn. Reson. Imaging*.
- Miller, D.H., 1994. Magnetic resonance in monitoring the treatment of multiple sclerosis.

- Ann. Neurol. 36, S91–94 (Suppl).
- Morrison, C., Henkelman, R.M., 1995. A model for magnetization transfer in tissues. *Magn. Reson. Med.* 33, 475–482.
- Odrobina, E.E., Lam, T.Y., Pun, T., Midha, R., Stanisz, G.J., 2005. MR properties of excised neural tissue following experimentally induced demyelination. *NMR Biomed.* 18, 277–284.
- Ou, X., Sun, S.W., Liang, H.F., Song, S.K., Gochberg, D.F., 2009a. The MT pool size ratio and the DTI radial diffusivity may reflect the myelination in shiverer and control mice. *NMR Biomed.* 22, 480–487.
- Ou, X., Sun, S.W., Liang, H.F., Song, S.K., Gochberg, D.F., 2009b. Quantitative magnetization transfer measured pool-size ratio reflects optic nerve myelin content in ex vivo mice. *Magn. Reson. Med.* 61, 364–371.
- Patrucco, L., Rojas, J.I., Cristiano, E., 2012. Assessing the value of spinal cord lesions in predicting development of multiple sclerosis in patients with clinically isolated syndromes. *J. Neurol.* 259, 1317–1320.
- Rausch, M., Tofts, P., Lervik, P., Walmsley, A., Mir, A., Schubart, A., Seabrook, T., 2009. Characterization of white matter damage in animal models of multiple sclerosis by magnetization transfer ratio and quantitative mapping of the apparent bound proton fraction f . *Mult. Scler.* 15, 16–27.
- Samsonov, A., Alexander, A.L., Mossahebi, P., Wu, Y.C., Duncan, I.D., Field, A.S., 2012. Quantitative MR imaging of two-pool magnetization transfer model parameters in myelin mutant shaking pup. *NeuroImage* 62, 1390–1398.
- Schmierer, K., Tozer, D.J., Scaravilli, F., Altmann, D.R., Barker, G.J., Tofts, P.S., Miller, D.H., 2007. Quantitative magnetization transfer imaging in postmortem multiple sclerosis brain. *J. Magn. Reson. Imaging* 26, 41–51.
- Sled, J.G., Pike, G.B., 2000. Quantitative interpretation of magnetization transfer in spoiled gradient echo MRI sequences. *J. Magn. Reson.* 145, 24–36.
- Sled, J.G., Pike, G.B., 2001. Quantitative imaging of magnetization transfer exchange and relaxation properties in vivo using MRI. *Magn. Reson. Med.* 46, 923–931.
- Smith, A.K., Dortch, R.D., Dethrage, L.M., Smith, S.A., 2014. Rapid, high-resolution quantitative magnetization transfer MRI of the human spinal cord. *NeuroImage* 95, 106–116.
- Stanisz, G.J., Odobina, E.E., Pun, J., Escaravage, M., Graham, S.J., Bronskill, M.J., Henkelman, R.M., 2005. T1, T2 relaxation and magnetization transfer in tissue at 3T. *Magn. Reson. Med.* 54, 507–512.
- Tozer, D., Ramani, A., Barker, G.J., Davies, G.R., Miller, D.H., Tofts, P.S., 2003. Quantitative magnetization transfer mapping of bound protons in multiple sclerosis. *Magn. Reson. Med.* 50, 83–91.
- Underhill, H.R., Rostomily, R.C., Mikheev, A.M., Yuan, C., Yarnykh, V.L., 2011. Fast bound pool fraction imaging of the in vivo rat brain: association with myelin content and validation in the C6 glioma model. *NeuroImage* 54, 2052–2065.
- Wolff, S.D., Balaban, R.S., 1989. Magnetization transfer contrast (MTC) and tissue water proton relaxation in vivo. *Magn. Reson. Med.* 10, 135–144.
- Yarnykh, V.L., 2002. Pulsed Z-spectroscopic imaging of cross-relaxation parameters in tissues for human MRI: theory and clinical applications. *Magn. Reson. Med.* 47, 929–939.
- Yarnykh, V.L., 2012. Fast macromolecular proton fraction mapping from a single off-resonance magnetization transfer measurement. *Magn. Reson. Med.* 68, 166–178.
- Yarnykh, V.L., Yuan, C., 2004. Cross-relaxation imaging reveals detailed anatomy of white matter fiber tracts in the human brain. *NeuroImage* 23, 409–424.
- Yarnykh, V.L., Bowen, J.D., Samsonov, A., Repovic, P., Mayadev, A., Qian, P., Gangadharan, B., Keogh, B.P., Maravilla, K.R., Jung Henson, L.K., 2015. Fast whole-brain three-dimensional macromolecular proton fraction mapping in multiple sclerosis. *Radiology* 274, 210–220.